

A Scaled Mesh/Nodal Formulation of Magnetic Equivalent Circuits with Motion

Daniel C. Horvath, *Student Member, IEEE*, Steven D. Pekarek, *Fellow, IEEE* and Scott D. Sudhoff, *Fellow, IEEE*

Abstract—In this research, a focus is on the efficient solution of magnetic equivalent circuits that include relative motion between components. It is shown that by combining the use of mesh and nodal analysis, one can avoid the need to restructure the circuit topology, which is a step encountered in strictly mesh-based approaches. In addition, one can overcome the poor convergence properties observed in strictly nodal-based formulations. A scaling of variables is introduced to ensure the condition number of the mixed mesh/nodal matrices remains relatively low. The proposed scaled model structure is then extended to MECs that are coupled to electrical systems for analysis of dynamic performance. It is shown that the numerical properties of the coupled scaled model remain strong.

Index Terms—Magnetic equivalent circuit, convergence, mesh analysis, nodal analysis, permeance, reluctance, condition number

pA	Matrix containing partial derivatives of nonlinear reluctances.
R_{cXi}	Reluctance of claw section Xi , $X \in \{1, 2\}$, $i \in \{1 \dots N\}$.
R_{si}	Reluctance of stator tooth i , $i \in \{1, 2\}$.
R_m	Reluctance of permanent magnet.
r	Resistance matrix.
u	Magnetic scalar potential.
v	Vector of winding voltages.
w	Width.
x	Solution vector of mixed mesh/nodal system.
x	Cartesian coordinate.
x'	Local Cartesian coordinate of claw section in x direction.
y	Cartesian coordinate.

NOMENCLATURE

δ	Change in a variable.
ζ	Per-unitized variable, $\zeta \in \{A, P, R, B, \phi, F\}$.
μ	Permeability.
κ	Condition number.
λ	Vector of winding flux linkages.
Φ	Total flux through flux tube.
ϕ	Loop flux.
φ	Vector of loop fluxes.
A	System matrix for mixed mesh/nodal formulation.
A	Area.
A_P	System matrix for nodal formulation.
A_R	System matrix for mesh formulation.
B	Magnetic flux density.
b	Input vector of mixed mesh/nodal system.
D	Difference matrix.
d	Displacement of claws from y -axis.
F	Vector of MMF sources.
F	Magneto-motive force (MMF) source.
g_m	Residual of mesh-based equation system.
g_n	Residual of nodal-based equation system.
H_c	Permanent magnet coercivity.
i	Vector of winding currents.
J	Jacobian matrix.
k	Iteration index of Newton-Raphson algorithm.
l	Length.
N	Number of claw sections in each claw.
P_{agi}	Permeance of airgap flux tube i .

D. C. Horvath S. D. Pekarek and S. D. Sudhoff are with the Department of Electrical and Computer Engineering, Purdue University, West Lafayette, IN, 47906 USA (e-mail: dhorvath@purdue.edu; spekarek@purdue.edu; sudhoff@purdue.edu).

Manuscript received October 6, 2017; revised November 28, 2017.

I. INTRODUCTION

MAGNETIC equivalent circuit (MEC) analysis is a well-established method of modeling electromagnetic and electromechanical components. Numerous researchers have explored their use in the analysis of electric machinery, inductors and transformers [1]–[6]. Interest in MECs has continued to grow with the emergence of population-based design (PBD) [7]–[11], wherein one is required to solve a model many times ($10^4 - 10^6$) in the search for optimal designs.

Traditionally, the challenges in utilizing MECs to numerically model systems with nonlinear magnetic materials have included the need for many iterations, the requirement of a relaxation factor to obtain convergence, or failure of convergence [12]–[14]. A component of the solution process is a system of equations established through circuit analysis techniques such as Kirchhoff's laws. Most commonly, Kirchhoff's Current Law (KCL), or nodal analysis, is applied at each node in the MEC [1]. In [13] and [14] the numerical stability of alternative MEC formulations based upon Kirchhoffs Voltage Law (KVL), or mesh analysis, was considered. Therein, it was shown that a formulation based upon KVL, wherein loop flux is used as the unknown, provides a computational advantage over a KCL-based formulation in terms of the number of iterations required to converge. This is attributed in part to the improved conditioning of the Jacobian matrix in the KVL formulation as well as the shape of the corresponding residual function [14].

Although KVL formulations have a numerical advantage in terms of convergence, they do provide a challenge to implement in systems with mechanical motion. Specifically, as parts of a magnetic system come out of relative alignment, loop reluctances approach infinite values, effectively

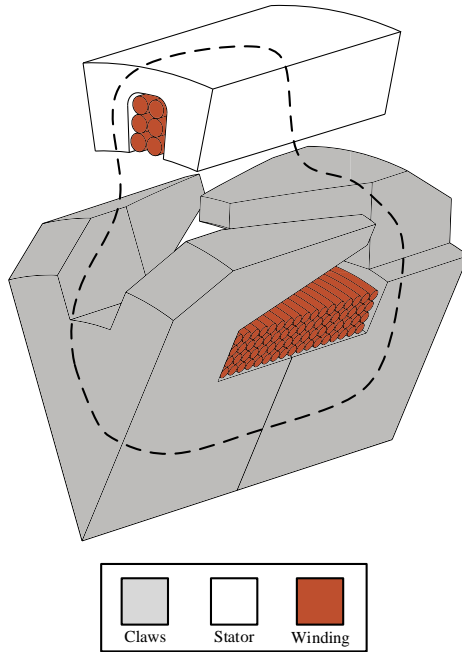


Fig. 1. Claw pole machine cutaway with dotted line indicating flux path.

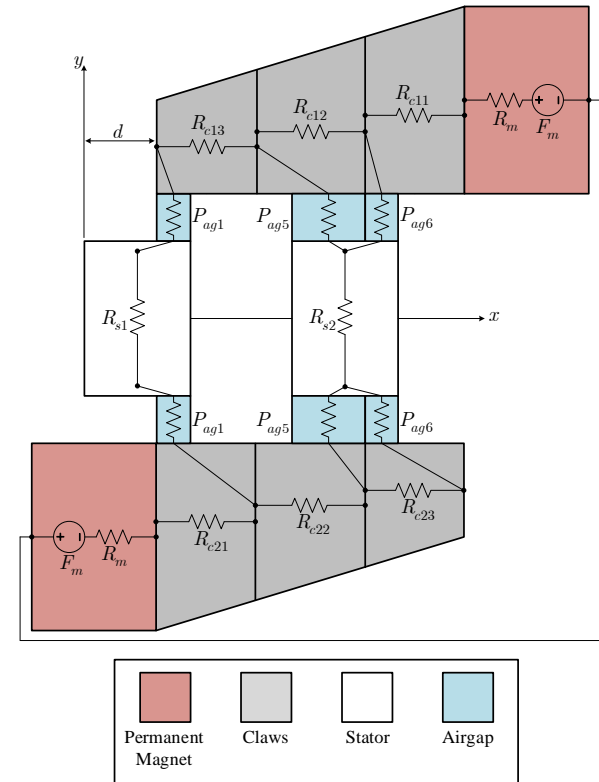


Fig. 2. Diagram of magnetic system representing mechanical motion.

breaking loops. An infinite reluctance in the system matrix is numerically infeasible, therefore the system of equations must be modified throughout the mechanical range of motion to remove the unknown flux variables associated with the infinite reluctance, effectively changing the circuit topology. In existing mesh analysis efforts, algorithms were developed for this purpose such as the “Shape Algorithm” set forth in [14] for salient pole wound rotor synchronous machines.

In this paper, a formulation is derived that maintains the strong convergence properties of the KVL formulation while maintaining the relative simplicity of the KCL formulation. Specifically, in this approach, the unknowns are the magnetic flux through nonlinear elements and node potentials at parts of the circuit that contain linear magnetic materials. In electric circuit analysis, researchers have combined KVL and KCL to take advantage of the respective strengths of each [15], [16]. Herein it is shown that such an approach is useful in MECs. In addition, it is shown that a per-unitization is needed to normalize the system of equations to eliminate the wide range in magnitude of matrix component values as a result of having both reluctance and permeance in the formulation. The numerical performance of the proposed formulation is then demonstrated through evaluation of a simplified claw-pole structure similar to that considered in [13]. Through this evaluation, it is shown that the condition number of the Jacobian matrix and the iteration count used in a Newton-Raphson (N-R) algorithm remain low over a wide range of magnetic operating conditions and relative positions of magnetic materials.

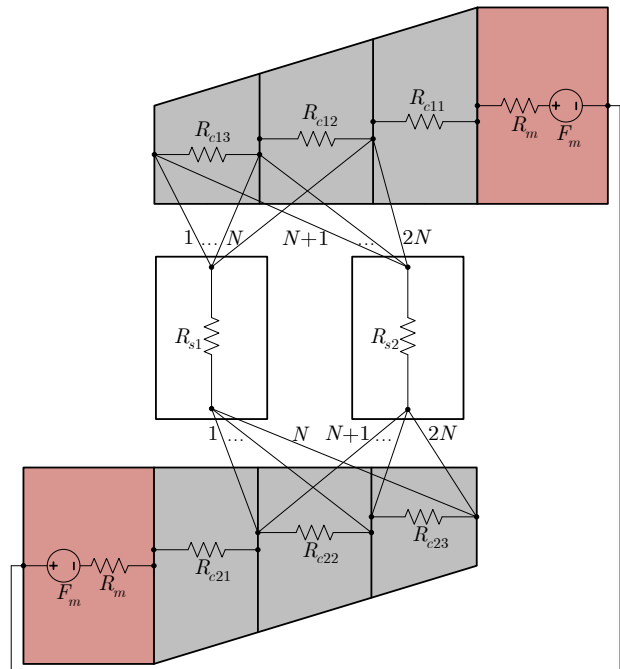


Fig. 3. Numbering of airgap elements while all possible airgap connections considered.

II. BACKGROUND

The magnetic structure studied in this research draws from that of a claw-pole alternator, primarily used in the automotive industry. A cutaway of such a claw-pole machine is provided in Fig. 1 in order to help understand the flux paths of the simplified structure considered in this paper. One notes that in such a machine, rotor excitation is provided by a field coil wrapped bobbin style along an axial core. The stator is a traditional structure with teeth/slot openings uniform along the axial direction.

The topology shown in Fig. 2 is based upon a simplified claw structure originally utilized in [13] to explore the numerical properties of MEC systems. The use of the structure was based upon the fact that the difference in convergence properties of alternative MEC formulations was first witnessed by an author of this paper in the study of a claw-pole machine. Explaining alternative formulations of the full claw-pole machine is tedious and therefore the simplified structure was used as a proxy. Comparing Figs. 1 and 2 one can observe that the magnetic excitation originally provided by a field winding is replaced with a permanent magnet that enables straightforward manipulation of the magnetic operating point. The leakage flux between claws is not represented. In addition, the complexity of the stator flux path is reduced by utilizing straight iron teeth between the claw halves. Furthermore, the axial flux path through the rotor core in Fig. 1 is simply modeled as a short circuit between the permanent magnet sources in Fig. 2.

In Fig. 2, x and y mark the coordinate axes. The variable d denotes the relative position between the claws and y -axis. An additional view of the magnetic system is provided in Fig. 3 in order to draw attention to the way the circuit equations are formed. In particular, one must consider all airgap elements to be simultaneously-connected and form the system of equations without assuming any disconnected airgap elements. In addition, the airgap element numbering is illustrated in Fig. 3. One notes that the claws have been discretized into N sections along the x direction. The diagrams and mathematical model developed herein use $N = 3$ for simplicity and compactness. In Section V N is adjusted in order to adjust the resolution of flux density distribution in the magnetic system.

III. CONVENTIONAL MEC ANALYSIS

Traditionally, the formulation of an MEC is based upon KCL applied to each node [1]. A circuit diagram is shown in Fig. 4 with nodal magnetic potential and loop flux definitions. If one considers the circuit nodes in Fig. 4, KCL can be applied at each node which results in a system of equations of the form

$$\mathbf{A}_P(\mathbf{u})\mathbf{u} = \boldsymbol{\varphi} \quad (1)$$

where the matrix \mathbf{A}_P contains linear combinations of permeances between the nodes in the circuit, \mathbf{u} contains unknown nodal magnetic potentials and $\boldsymbol{\varphi}$ contains flux sources. An alternative formulation of an MEC is based upon KVL applied to circuit loops. If one considers the circuit loops in Fig. 4,

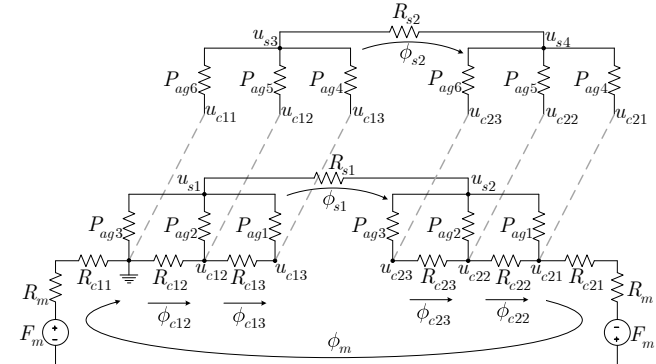


Fig. 4. Circuit diagram with unknown potentials and fluxes.

KVL can be applied which results in a system of equations of the form

$$\mathbf{A}_R(\boldsymbol{\varphi})\boldsymbol{\varphi} = \mathbf{u} \quad (2)$$

where the matrix \mathbf{A}_R contains linear combinations of reluctances which the loop fluxes flow through, $\boldsymbol{\varphi}$ contains unknown loop fluxes and \mathbf{u} contains MMF sources. If the magnetic material is linear, either (1) or (2) will provide identical results (to machine precision). However, it has been shown that for magnetic material that is nonlinear, the KVL formulation (2) has superior numerical properties compared to the KCL formulation (1). Specifically, as shown in [13] the solution of (2) can be obtained with a N-R algorithm requiring relatively few iterations, without a need for relaxation. This is attributed to two issues with the KCL formulation. One, the resulting Jacobian matrix tends to have very large condition numbers. In addition, the shape of the residual function is such that convergence is more difficult to achieve. To briefly consider herein, the nodal and mesh formulation results in residual functions of the form:

$$g_n(\mathbf{u}) = \mathbf{A}_P(\mathbf{u})\mathbf{u} - \boldsymbol{\varphi} = \mathbf{0} \quad (3)$$

$$g_m(\boldsymbol{\varphi}) = \mathbf{A}_R(\boldsymbol{\varphi})\boldsymbol{\varphi} - \mathbf{u} = \mathbf{0} \quad (4)$$

The shape of the these functions for single variable systems was presented in [14] and is revisited here. A plot of an example residual function for a single-variable nodal system is shown in Fig. 5. As shown, the nodal solution begins at some initial point $u^{(1)}$. From $u^{(1)}$, the solution for the next iteration, $u^{(2)}$, is determined using the tangent line at the point $u^{(1)}$. As the process repeats, it is apparent that the succession of iterations will begin to diverge away from u^* . In contrast, a plot of an example residual function for a single-variable mesh system is shown in Fig. 6. The succession of iterations in an N-R algorithm for the mesh residual tends to converge to the true solution ϕ^* . Although formulation (2) has numerical advantages, when one considers electromechanical devices capable of motion, the formulation of (1) has an inherent simplicity as opposed to (2). Specifically, with formulation (1), as stator teeth/claws come out of relative alignment, the respective permeance values will approach zero. In contrast, considering (2), when stator teeth/rotor claws come out of

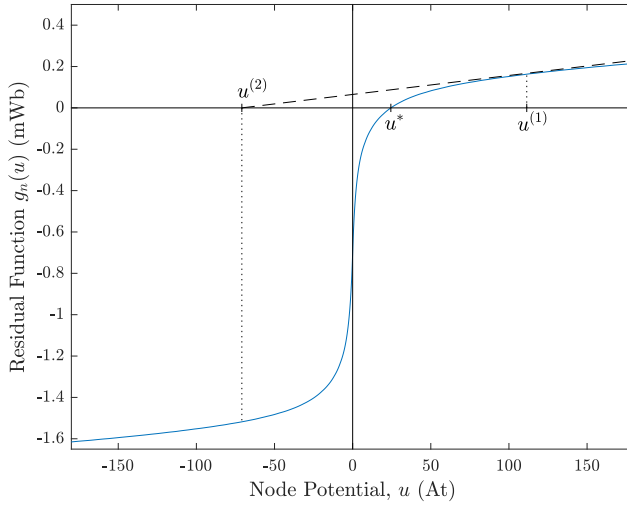


Fig. 5. Nodal-based solution procedure.

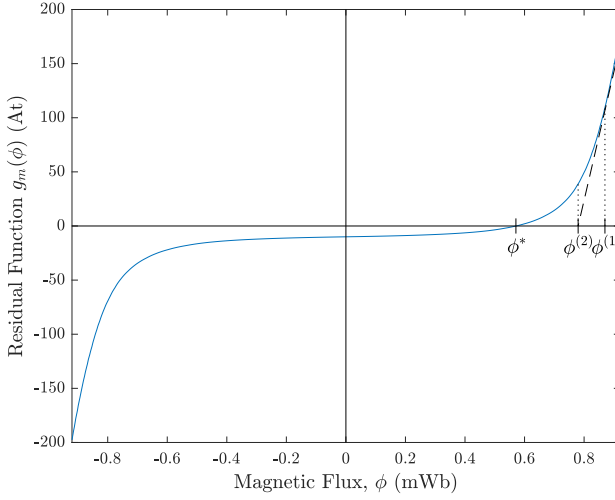


Fig. 6. Mesh-based solution procedure.

alignment, the respective reluctance values become infinite. As a result, one is forced to keep track of reluctance values and reformulate the system of equations as reluctances become large. Additionally, MECs often contain many flux paths in the airgaps. Thus, mesh analysis requires the identification of all loops in the circuit, which can be difficult to determine as the number of circuit components increases, especially if the circuit cannot be represented in a planar fashion.

In this research, a mixed mesh/nodal system of equations is formed that offers the advantages of both methods of circuit analysis. Namely, the solution does not require relaxation, nor does it require one to keep track of reluctance values and restructure the circuit topology at each mechanical position.

IV. SCALED MESH/NODAL MEC ANALYSIS

A. Establishing Unknowns

The circuit diagram representing the MEC for the system considered is shown in Fig. 4. In the proposed mixed mesh/nodal formulation, the flux through nonlinear elements

along with the essential nodes are taken as the unknowns of the system. As an example, referencing Fig. 4, KCL is applied at node u_{s1} yielding the nodal equation:

$$\begin{aligned} \phi_{s1} + u_{s1}P_{ag3} + (u_{s1} - u_{c12})P_{ag2} \\ + (u_{s1} - u_{c13})P_{ag1} = 0 \end{aligned} \quad (5)$$

It is noted that (5) is a linear equation because the permeability in airgap permeance elements depends neither on nodal potentials nor loop fluxes. Indeed, all nodal equations are linear in the proposed formulation. Herein, the term essential is used to refer to the fact that not all nodes in the circuit are used. For example, the node between series elements is not labeled. Applying KVL around the loop involving ϕ_m in Fig. 4, the following mesh equations results:

$$\phi_m(R_{c11}(\phi_m) + R_{c21}(\phi_m) + 2R_m) - u_{c21} = 2F_m \quad (6)$$

Note that (6) is a nonlinear equation because of the dependence of the claw section reluctances on the loop flux. Within the formulation, the system of unique equations is represented as

$$\begin{bmatrix} \mathbf{A}_R(\varphi) & \mathbf{D}_1 \\ \mathbf{D}_2 & \mathbf{A}_P \end{bmatrix} \begin{bmatrix} \varphi \\ \mathbf{u} \end{bmatrix} = \begin{bmatrix} \mathbf{F} \\ \mathbf{0} \end{bmatrix} \quad (7)$$

The relevant reluctance or permeance expressions for the flux tubes are given in the Appendix.

$$\mathbf{A}_R(\varphi) = \begin{bmatrix} R_M & 0 & 0 & 0 & 0 & 0 & 0 \\ 0 & R_{s1} & 0 & 0 & 0 & 0 & 0 \\ 0 & 0 & R_{s2} & 0 & 0 & 0 & 0 \\ 0 & 0 & 0 & R_{c12} & 0 & 0 & 0 \\ 0 & 0 & 0 & 0 & R_{c13} & 0 & 0 \\ 0 & 0 & 0 & 0 & 0 & R_{c22} & 0 \\ 0 & 0 & 0 & 0 & 0 & 0 & R_{c23} \end{bmatrix} \quad (8)$$

$$\mathbf{D}_1 = \begin{bmatrix} 0 & 0 & 0 & 0 & 0 & 0 & -1 & 0 & 0 \\ -1 & 1 & 0 & 0 & 0 & 0 & 0 & 0 & 0 \\ 0 & 0 & -1 & 1 & 0 & 0 & 0 & 0 & 0 \\ 0 & 0 & 0 & 0 & 1 & 0 & 0 & 0 & 0 \\ 0 & 0 & 0 & 0 & -1 & 1 & 0 & 0 & 0 \\ 0 & 0 & 0 & 0 & 0 & 0 & 1 & -1 & 0 \\ 0 & 0 & 0 & 0 & 0 & 0 & 0 & 1 & -1 \end{bmatrix} \quad (9)$$

$$\mathbf{D}_2 = \begin{bmatrix} 0 & 1 & 0 & 0 & 0 & 0 & 0 & 0 \\ 0 & -1 & 0 & 0 & 0 & 0 & 0 & 0 \\ 0 & 0 & 1 & 0 & 0 & 0 & 0 & 0 \\ 0 & 0 & -1 & 0 & 0 & 0 & 0 & 0 \\ 0 & 0 & 0 & -1 & 1 & 0 & 0 & 0 \\ 0 & 0 & 0 & 0 & 0 & 1 & -1 & 0 \\ 0 & 0 & 0 & 0 & 0 & 0 & 0 & 1 \\ 0 & 0 & 0 & 0 & 0 & 0 & 0 & 1 \end{bmatrix} \quad (10)$$

$$R_M = R_{c11} + R_{c21} + 2R_m \quad (12)$$

$$\varphi = [\phi_m \quad \phi_{s1} \quad \phi_{s2} \quad \phi_{c12} \quad \phi_{c13} \quad \phi_{c22} \quad \phi_{c23}]^T \quad (13)$$

$$\mathbf{u} = [\mathbf{u}_S \quad \mathbf{u}_C]^T \quad (14)$$

$$\mathbf{A}_P = \begin{bmatrix} \sum_{i=1}^N P_{agi} & 0 & 0 & 0 & -P_{ag2} & -P_{ag1} & 0 & 0 & 0 \\ 0 & \sum_{i=1}^N P_{agi} & 0 & 0 & 0 & 0 & -P_{ag1} & -P_{ag2} & -P_{ag3} \\ 0 & 0 & \sum_{i=N+1}^{2N} P_{agi} & 0 & -P_{ag5} & -P_{ag4} & 0 & 0 & 0 \\ 0 & 0 & 0 & \sum_{i=N+1}^{2N} P_{agi} & 0 & 0 & -P_{ag4} & -P_{ag5} & -P_{ag6} \\ -P_{ag2} & 0 & -P_{ag5} & 0 & \frac{P_{ag2}}{+P_{ag5}} & 0 & 0 & 0 & 0 \\ -P_{ag1} & 0 & -P_{ag4} & 0 & 0 & \frac{P_{ag1}}{+P_{ag4}} & 0 & 0 & 0 \\ 0 & -P_{ag1} & 0 & -P_{ag4} & 0 & 0 & \frac{P_{ag1}}{+P_{ag4}} & 0 & 0 \\ 0 & -P_{ag2} & 0 & -P_{ag5} & 0 & 0 & 0 & \frac{P_{ag2}}{+P_{ag5}} & 0 \\ 0 & -P_{ag3} & 0 & -P_{ag6} & 0 & 0 & 0 & 0 & \frac{P_{ag3}}{+P_{ag6}} \end{bmatrix} \quad (11)$$

$$\mathbf{u}_S = [u_{s1} \ u_{s2} \ u_{s3} \ u_{s4}] \quad (15)$$

$$\mathbf{u}_C = [u_{c12} \ u_{c13} \ u_{c21} \ u_{22} \ u_{23}] \quad (16)$$

$$\mathbf{F} = [2F_m \ 0 \ 0 \ 0 \ 0 \ 0 \ 0]^T \quad (17)$$

The system of equations (7), written more generally as $\mathbf{A}(\mathbf{x})\mathbf{x} = \mathbf{b}$, is rearranged to form a residual function to which a particular input vector \mathbf{x} is sought that will zero the output.

$$g(\mathbf{x}) = \mathbf{A}(\mathbf{x})\mathbf{x} - \mathbf{b} = \mathbf{0} \quad (18)$$

In applying an N-R algorithm to solve (18), it has been observed that the resulting Jacobian matrix is often ill-conditioned (the condition number for inversion is on the order of 10^{15}). Ill-conditioned Jacobian matrices may prevent the N-R algorithm from converging due to the sensitivity of each linear N-R step [17]. The high condition number in the mixed system is due to a large disparity in the magnitudes of the reluctances and permeances which appear in the Jacobian matrix. In order to circumvent this issue, a scaling is applied to the system of equations using a per-unitization type of variable transformation.

B. Definition of Per-Unit System

At each rotor position, the airgap permeance cross-sectional areas are determined by examination of the relative alignment between the claw sections and stator teeth, as described in the appendix. The maximum of these areas is taken as the base area:

$$A_{base} \triangleq \max(\mathbf{A}_{airgap}) \quad (19)$$

where \mathbf{A}_{airgap} is the vector of the airgap permeance areas. From the base area, a base value of permeance is defined:

$$P_{base} \triangleq \mu_0 \frac{A_{base}}{g} \quad (20)$$

which also yields a base value for reluctance through the reciprocal relationship:

$$R_{base} \triangleq \frac{1}{P_{base}} \quad (21)$$

Subsequently, a base value of flux density is selected. This value can be arbitrarily chosen. In this research, it has been selected as a value near the knee of the saturation curve ($B_{base} \triangleq 1.6$ T). From these, the remaining base quantities are defined:

$$\phi_{base} \triangleq B_{base} A_{base} \quad (22)$$

$$F_{base} \triangleq \phi_{base} R_{base} \quad (23)$$

For all quantities, the relationship between actual variables and their per-unit counterparts is

$$\hat{\zeta} = \frac{\zeta}{\zeta_{base}} \quad (24)$$

where $\zeta \in \{A, P, R, B, \phi, F\}$ and the hat notation is used to denote variables that are in per-unit. Using (24), (7) can be expressed in a per-unit form as:

$$\begin{bmatrix} \hat{\mathbf{A}}_R(\hat{\phi}) & \mathbf{D}_1 \\ \mathbf{D}_2 & \hat{\mathbf{A}}_P \end{bmatrix} \begin{bmatrix} \hat{\phi} \\ \hat{\mathbf{u}} \end{bmatrix} = \begin{bmatrix} \hat{\mathbf{F}} \\ \mathbf{0} \end{bmatrix} \quad (25)$$

To illustrate further, equation (6) can be converted to per-unit by first dividing all terms by F_{base} :

$$\frac{\phi_m (R_{c11} + R_{c21} + 2R_m)}{F_{base}} - \frac{u_{c21}}{F_{base}} = \frac{2F_m}{F_{base}} \quad (26)$$

Subsequently, by using the relationships (23) and (24), (26) can be expressed in per-unit as

$$\hat{\phi}_m (\hat{R}_{c11}(\hat{\phi}_m) + \hat{R}_{c21}(\hat{\phi}_m) + 2\hat{R}_m) - \hat{u}_{c21} = 2\hat{F}_m \quad (27)$$

A similar approach is taken with the nodal equations where each term is divided by ϕ_{base} . It is noted that following scaling, each term in the system matrix has similar magnitude.

This example also illustrates how the matrices D_1 and D_2 remain unchanged, which is not possible with a simple row-based scaling approach. Consequently, the per-unit conversion from (7) to (25) significantly reduces the condition number of the associated Jacobian matrix, as will be shown in the following section.

C. Solution of the Scaled System

With the system of equations scaled, the Jacobian matrix for the residual function is readily derived. The residual function for the per-unit system is now

$$\hat{g}(\hat{x}) = \hat{A}(\hat{x})\hat{x} - \hat{b} \quad (28)$$

and the N-R iterator is

$$\hat{x}^{k+1} = \hat{x}^k - [\hat{J}(\hat{x}^k)]^{-1} \hat{g}(\hat{x}^k) \quad (29)$$

where k denotes the iteration and $\hat{J}(\hat{x}^k)$ denotes the Jacobian matrix of the per-unit system evaluated at iteration k . The first entry in the Jacobian matrix is obtained by rearranging (27) and differentiating

$$\begin{aligned} \hat{J}_{11} &= \frac{\partial \hat{g}_1(\hat{x})}{\partial \hat{\phi}_m} = \left(\hat{R}_{c11} + \hat{R}_{c21} + 2\hat{R}_m \right) \\ &\quad + \hat{\phi}_m \left(\frac{\partial \hat{R}_{c11}}{\partial \hat{\phi}_m} + \frac{\partial \hat{R}_{c21}}{\partial \hat{\phi}_m} \right) \end{aligned} \quad (30)$$

The partial derivative terms are resolved using the chain rule. For example,

$$\begin{aligned} \frac{\partial \hat{R}_{c11}}{\partial \hat{\phi}_m} &= \frac{\phi_{base}}{R_{base}} \frac{\partial R_{c11}}{\partial \phi_m} \\ &= \frac{\phi_{base}}{R_{base}} \frac{\partial R_{c11}}{\partial \mu_{c11}} \frac{\partial \mu_{c11}}{\partial B_{c11}} \frac{\partial B_{c11}}{\partial \Phi_{c11}} \frac{\partial \Phi_{c11}}{\partial \phi_m} \end{aligned} \quad (31)$$

where Φ_{c11} denotes the total flux through element R_{c11} . Several expressions are needed for each term in the right hand side of (31). The per-unit bases are known and their selection is described in Section IV. Since μ_{c11} appears in the denominator of the reluctance expression for element R_{c11} (listed in the appendix), the second term can be written as

$$\frac{\partial R_{c11}}{\partial \mu_{c11}} = -\frac{1}{\mu_{c11}} R_{c11} \quad (32)$$

The term $\partial \mu_{rc11}/\partial B_{c11}$ is determined from the material's interpolated μ -B characteristic. Since $B_{c11} = \Phi_{c11}/A_{c11}$,

$$\frac{\partial B_{c11}}{\partial \Phi_{c11}} = \frac{1}{A_{c11}} \quad (33)$$

From Fig. 4, $\Phi_{c11} = \phi_m$. Therefore,

$$\frac{\partial \Phi_{c11}}{\partial \phi_m} = 1 \quad (34)$$

An analytical expression for (31) is then established as

$$\frac{\partial \hat{R}_{c11}}{\partial \hat{\phi}_m} = -\frac{\phi_{base}}{R_{base}} \frac{R_{c11}}{\mu_{rc11} A_{c11}} \frac{\partial \mu_{rc11}}{\partial B_{c11}} \quad (35)$$

It is noted that the first term in \hat{J}_{11} also appears in the first entry of $\hat{A}_R(\hat{\phi})$, and the general form of the Jacobian matrix is a sum of terms from \hat{A} and their partial derivatives

$$\hat{J} = \hat{A} + \hat{p}\hat{A} \quad (36)$$

where the remaining partial derivative terms reside in the matrix $\hat{p}\hat{A}$. For the mixed system,

$$\hat{p}\hat{A} = \begin{bmatrix} \hat{p}\hat{A}_R & \mathbf{0} \\ \mathbf{0} & \mathbf{0} \end{bmatrix} \quad (37)$$

The matrix $\hat{p}\hat{A}_R$ is a diagonal matrix whose entries are the following:

$$\hat{p}\hat{A}_{R,11} = \frac{\partial \hat{R}_{c11}}{\partial \hat{\phi}_m} \hat{\phi}_m + \frac{\partial \hat{R}_{c21}}{\partial \hat{\phi}_m} \hat{\phi}_m \quad (38)$$

$$\hat{p}\hat{A}_{R,22} = \frac{\partial \hat{R}_{s1}}{\partial \hat{\phi}_{s1}} \hat{\phi}_{s1} \quad (39)$$

$$\hat{p}\hat{A}_{R,33} = \frac{\partial \hat{R}_{s2}}{\partial \hat{\phi}_{s2}} \hat{\phi}_{s2} \quad (40)$$

$$\hat{p}\hat{A}_{R,44} = \frac{\partial \hat{R}_{c12}}{\partial \hat{\phi}_{c12}} \hat{\phi}_{c12} \quad (41)$$

$$\hat{p}\hat{A}_{R,55} = \frac{\partial \hat{R}_{c13}}{\partial \hat{\phi}_{c13}} \hat{\phi}_{c13} \quad (42)$$

$$\hat{p}\hat{A}_{R,66} = \frac{\partial \hat{R}_{c22}}{\partial \hat{\phi}_{c22}} \hat{\phi}_{c22} \quad (43)$$

$$\hat{p}\hat{A}_{R,77} = \frac{\partial \hat{R}_{c23}}{\partial \hat{\phi}_{c23}} \hat{\phi}_{c23} \quad (44)$$

The solution vector x contains two sets of variables, each of different units and thus since the magnitude of node potentials is typically orders of magnitude larger than magnetic flux, the nodal potentials may dominate the solution. By per-unitizing, the elements of the solution vector are unitless, and of similar magnitude, preventing domination. Within the N-R algorithm, the change in the norm of the solution vector is often used as the basis of a terminating condition for iteration. In this research, the airgap flux densities are computed at each iteration and the difference in the 2-norm between iterations is chosen as the stopping measure. More specifically, the N-R iteration is performed until

$$\|B_{airgap}^k - B_{airgap}^{k-1}\|_2 < 1 \times 10^{-6} \quad (45)$$

By selecting (45) as the N-R termination criterion, a direct comparison can be made between algorithms in terms of iteration counts.

V. COMPARISON OF METHODS

The system represented in Figs. 2-4 was simulated with geometric parameter values given in Table I and defined in Fig. 7. The parameters are similar to those of a single pole pair of an automotive alternator designed for a 12 V charging system in a passenger vehicle. The material considered for use in the claws and stator teeth exhibits a similar nonlinear relationship between field intensity and flux density as in [13]. To utilize within the MEC formulations, the B - H relationship

TABLE I
PHYSICAL DIMENSIONS OF MAGNETIC STRUCTURE

Dimension	Value
g	0.30 mm
d_{sys}	10.00 mm
w_{root}	11.50 mm
w_{tip}	3.00 mm
w_{stat}	7.00 mm
w_{slot}	6.00 mm
l_{claw}	27.00 mm
l_{stat}	11.50 mm
t_{mag}	1.00 mm

TABLE II
COMPUTATIONAL PERFORMANCE - PROPOSED SCALED MESH/NODAL MODEL ($d = 0$ mm)

H_c	Iterations	$\max(\mathbf{B})$	$\max(\kappa(\mathbf{J}))$
1.00×10^5 A/m	4	0.13 T	5.03×10^2
8.00×10^5 A/m	5	1.00 T	5.03×10^2
1.60×10^6 A/m	6	1.90 T	5.03×10^2
2.00×10^6 A/m	6	2.26 T	5.03×10^2
2.40×10^6 A/m	7	2.59 T	5.03×10^2
2.80×10^6 A/m	7	2.91 T	5.03×10^2

is recast into a μ - B relationship, utilized in each iteration of the N-R algorithm to update the nonlinear reluctances. The μ - B and $\partial\mu/\partial B$ relationships, interpolated using splines, are both utilized in the analytical Jacobian matrix entries. The material characteristics are further detailed in the appendix.

Herein a comparison is made between the proposed scaled mesh/nodal formulation and the conventional nodal formulation in terms of computational performance. In all methods, the permanent magnet coercivity is varied, effectively creating magnets of varying strength, so as to drive the magnetic flux density in the circuit to different values. The computational performance of the proposed scaled mesh/nodal solution is documented in Table II. The computational performance of two versions of the conventional nodal solution are presented in Tables III and IV. To establish Table III, the solution is implemented with an approximate Jacobian matrix as suggested in [13]. To establish Table IV, the full Jacobian matrix is utilized. In Tables II-IV, iteration counts are documented in the second column. In the third column, the maximum flux density throughout the MEC is listed. The condition number of the Jacobian matrix is stored throughout the solution iteration and the maximum value encountered is listed in the fourth column. Considering iteration counts of the conventional methods, it is clear that they increase with flux density and eventually fail to converge. In the proposed scaled mesh/nodal method the iteration counts stay relatively fixed and converge reliably. Indeed, one can observe that the maximum flux density is 2.91 T in Table II, which is well beyond the saturation knee of 1.6 T shown in Fig. 11 and yet the iteration count remains relatively low.

A 2-D system diagram in the first subplot of in Fig. 8 while the flux density in the airgap for each respective model

TABLE III
COMPUTATIONAL PERFORMANCE - NODAL MODEL WITH APPROXIMATE JACOBIAN ($d = 0$ mm)

H_c	Iterations	$\max(\mathbf{B})$	$\max(\kappa(\mathbf{J}))$
1.00×10^5 A/m	4	0.13 T	4.90×10^5
8.00×10^5 A/m	6	1.00 T	4.90×10^5
1.60×10^6 A/m	18	1.90 T	4.90×10^5
2.00×10^6 A/m	35	2.26 T	4.90×10^5
2.40×10^6 A/m	Did not converge		
2.80×10^6 A/m	Did not converge		

formulation is shown the second subplot. The flux density in each claw section is shown in the third subplot of Fig. 8. Note that in the upper claw the rightmost claw section is section 1, having reluctance R_{c11} .

To provide confidence in the accuracy of the proposed MEC formulation, a 2-D Finite Element (FE) model of the structure was created with the commercial package ANSYS Maxwell. In the FE model, the same anhysteretic nonlinear B-H characteristic shown in Fig. 11 was used in the claws and stator teeth. To be consistent with the proxy machine in which leakage paths are not represented, in the FE model the relative permeability of the material surrounding the magnetic structure was set to be $\mu_r = 1 \times 10^{-6}$. Similarly, the relative permeability of the material used between claws and stator teeth was set to $\mu_r = 1$, representing airgap elements. The short circuit connection between permanent magnet sources was modeled with a magnetic material path with relative permeability $\mu_r = 1 \times 10^{12}$. The results yielded by FE analysis are shown in Fig. 8 for the same operating conditions used to generate the MEC results.

Fig. 9 shows the airgap flux density for varying displacements between stator and claws when the coercivity is held fixed at $H_c = 2.40 \times 10^6$ A/m. Table V shows the iteration count and condition number of the Jacobian matrix at the same displacements used in Fig. 9. One notes that the flux density is in excess of 3 T when $d = 5.60$ mm and yet the iteration count

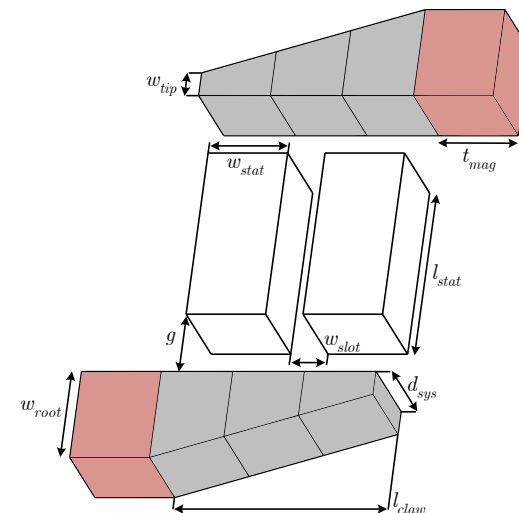


Fig. 7. System diagram with dimensions.

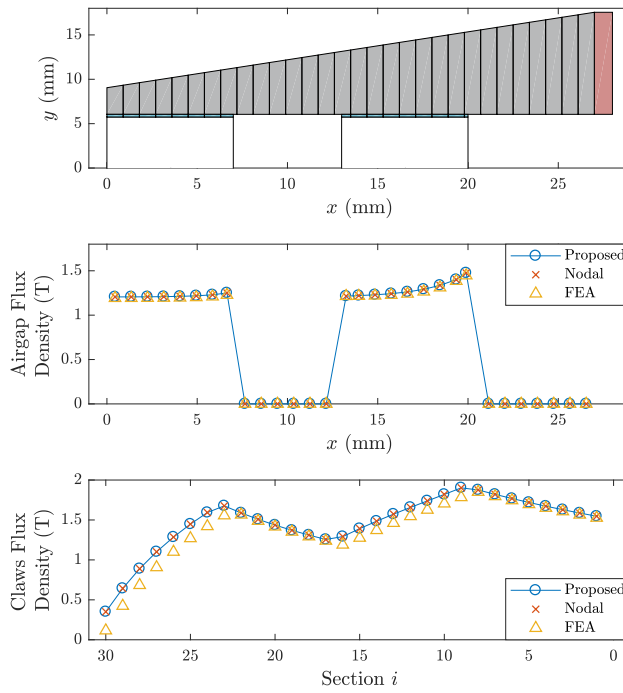


Fig. 8. Flux density in MEC ($H_c = 1.60 \times 10^6$ A/m, $d = 0.00$ mm, $N = 30$).

remains reasonably low. In addition, the condition numbers of the Jacobian matrices are kept to reasonable values under various flux density levels and displacements. One can argue that a general diagonal scaling or preconditioning approach can be used in place of the proposed per-unit scaling approach to improve the condition number. However the per-unit scaling offers a straightforward procedure for the selection of the scaling values, and is performed with little additional computational effort, i.e. without matrix multiplication.

The condition number of a matrix is often used as a measure of sensitivity to changes in the input vector \mathbf{b} when solving the general linear problem $\mathbf{Ax} = \mathbf{b}$. In particular,

$$\frac{\|\delta\mathbf{x}\|}{\|\mathbf{x}\|} \leq \kappa(\mathbf{A}) \frac{\|\delta\mathbf{b}\|}{\|\mathbf{b}\|} \quad (46)$$

where $\delta\mathbf{b}$ represents a change in the input, $\kappa(\mathbf{A})$ is the condition number of \mathbf{A} and $\delta\mathbf{x}$ is the corresponding change in the solution vector. Similarly, in the k^{th} iteration of the N-R

TABLE IV
COMPUTATIONAL PERFORMANCE - NODAL MODEL WITH ANALYTICAL JACOBIAN ($d = 0$ mm)

H_c	Iterations	$\max(\mathbf{B})$	$\max(\kappa(\mathbf{J}))$
1.00×10^5 A/m	5	0.13 T	4.90×10^5
8.00×10^5 A/m	Did not converge		
1.60×10^6 A/m	Did not converge		
2.00×10^6 A/m	Did not converge		
2.40×10^6 A/m	Did not converge		
2.80×10^6 A/m	Did not converge		

algorithm, the sensitivity of the linear solution to $\mathbf{J}^k \Delta \mathbf{x}^k = -\mathbf{g}^k$ is measured by

$$\frac{\|\delta\Delta\mathbf{x}^k\|}{\|\Delta\mathbf{x}^k\|} \leq \kappa(\mathbf{J}^k) \frac{\|\delta\mathbf{g}^k\|}{\|\mathbf{g}^k\|} \quad (47)$$

where in the N-R algorithm, $\Delta\mathbf{x}^k = \mathbf{x}^{k+1} - \mathbf{x}^k$. A large condition number does not guarantee a correspondingly large change in solution, but rather bounds it. In the system considered in this paper, the Jacobian matrix condition number of the unscaled mixed mesh/nodal model is on the order of 10^{15} . Comparing this to the scaled version (condition number on the order of 10^2), it is clear that the sensitivity bound is greatly reduced.

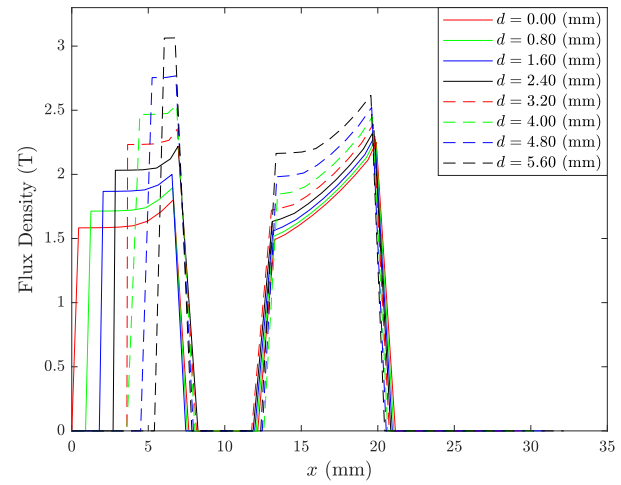


Fig. 9. Flux density in airgap ($H_c = 2.40 \times 10^6$ A/m).

TABLE V
COMPUTATIONAL PERFORMANCE IN MOTION ($H_c = 2.40 \times 10^6$ A/m)

d (mm)	Iterations	$\max(\kappa(\mathbf{J}))$
0.00	7	5.03×10^2
0.80	7	4.65×10^2
1.60	6	4.31×10^2
2.40	6	4.08×10^2
3.20	6	4.03×10^2
4.00	6	4.04×10^2
4.80	6	4.05×10^2
5.60	6	4.07×10^2

VI. EXTENSION TO DYNAMIC SIMULATIONS

The previous sections highlight an MEC solution in which the electrical dynamics between winding voltage and winding current are not considered. Such a model is heavily used in the design of electromagnetic components [5], [9], [18]–[24], and thus having an approach that minimizes numerical issues is important. Still, there are many instances in which the coupled electrical-magnetic dynamics are of interest [1], [4], [12], [18], [25]–[27]. Several researchers have explored techniques to solve dynamic MECs [1], [4], [12], [27]. In one approach, analytical methods are used to convert the algebraic

circuit model into additional states (i.e. node potentials of the MEC are among the state variables). This eliminates the need to use an algebraic solver (AS) and thus problems associated with AS convergence. An alternative to the formation of a strict state model is to form a strictly algebraic model by discretizing the state equations using, for example, a backward differentiation formula [28]. The resulting discretized equations are then solved together with the algebraic system using an AS. This approach was applied to nodal-based MECs in [4], [12]. Therein, the lack of convergence of the AS was documented as an issue and the use of specialized algorithms (i.e. Globally Convergent N-R) to improve convergence was proposed. Herein, the dynamic MEC was structured so that the algebraic MEC is used to establish the derivatives of state variables (winding flux linkages). The derivatives of the state variables are then used as inputs to the respective ODE solvers. To demonstrate this method, the magnetic structure was modified so that the two permanent magnets were replaced with a single field coil, which we assume to have the same series reluctance as the permanent magnets. The field coil consists of $N_{fd} = 300$ turns, with a resistance of $200\text{ m}\Omega$. From Faraday's law, the single state equation of the dynamic system can be expressed as

$$\frac{d}{dt}\lambda_{fd} = v_{fd} - r_{fd}i_{fd} \quad (48)$$

For the algebraic system, the per-unit MEC is reformulated to accept per-unit field winding flux linkage as a model input, and winding current (MMF) as an additional unknown. This yields:

$$\begin{bmatrix} \hat{\mathbf{A}}_R(\hat{\varphi}) & \mathbf{D}_1 & -N_{fd} \\ \mathbf{D}_2 & \hat{\mathbf{A}}_P & \mathbf{0} \\ 1 & \mathbf{0} & 0 \end{bmatrix} \begin{bmatrix} \hat{\varphi} \\ \hat{\mathbf{u}} \\ \hat{i}_{fd} \end{bmatrix} = \begin{bmatrix} \mathbf{0} \\ \mathbf{0} \\ 1/N_{fd} \end{bmatrix} \hat{\lambda}_{fd} \quad (49)$$

where $\hat{\lambda}_{fd} = \lambda_{fd}/\phi_{base}$ and $\hat{i}_{fd} = i_{fd}/F_{base}$. The iterative solution of (49) enables the calculation of the time derivative of state (48). The solution was implemented within MATLAB utilizing the built-in ODE solvers. Explicit, implicit, stiff and nonstiff solvers were applied. For each, the dynamic study considered was one in which the rotor is held fixed at $d = 0\text{ mm}$. The field voltage is initially set to $v_{fd} = 1\text{ V}$, which is a value that produces a magnetic operating point much below saturation in all flux tubes. The field voltage is then stepped to a value of $v_{fd} = 5\text{ V}$ at $t = 20\text{ ms}$ as shown in Fig. 10(a). For all fixed-step solvers, a time step of 1 ms was utilized. For all variable-step ODE solvers, a maximum time-step of 5 ms was utilized and the relative error tolerance was set to 1×10^{-3} . As noted within the static MEC, the NR algorithm was applied without the use of a relaxation factor. For all ODE solvers, the behavior of the AS was strong with iteration counts never greater than 7. The predicted response of the dynamic system was identical (neglecting slight numerical differences) in all cases. For the case in which the "ode23t" solver was used, the field current response is shown in Fig. 10(b). The flux density in claw section 1 is shown in Fig. 10(c). The iteration count of the NR solve is shown in Fig. 10(d). The maximum condition number of the per-unit Jacobian matrix, $\max(\kappa(\hat{\mathbf{J}}))$, was stored throughout the simulations and was found to hold

fixed at a value of 498 for all solvers. For the variable-step solvers, the "ode23tb" solver yielded the highest average time step of 4.55 ms throughout the time-domain simulation.

For magnetic devices with multiple windings, the system can be modeled dynamically with the following general algebraic system and ODE system:

$$\begin{bmatrix} \hat{\mathbf{A}}_R(\hat{\varphi}) & \mathbf{D}_1 & \mathbf{W}_1 \\ \mathbf{D}_2 & \hat{\mathbf{A}}_P & \mathbf{0} \\ \mathbf{W}_2 & \mathbf{0} & \mathbf{0} \end{bmatrix} \begin{bmatrix} \hat{\varphi} \\ \hat{\mathbf{u}} \\ \hat{\mathbf{i}} \end{bmatrix} = \begin{bmatrix} \mathbf{0} \\ \mathbf{0} \\ \mathbf{W}_3 \end{bmatrix} \hat{\lambda} \quad (50)$$

$$\frac{d}{dt}\hat{\lambda} = \mathbf{v} - \mathbf{r}\hat{\mathbf{i}} \quad (51)$$

where $\mathbf{W}_1\text{-}\mathbf{W}_3$ contain winding pattern information, similar to that presented in [18].

VII. CONCLUSION

In this paper, a solution for MECs is proposed for analysis of systems with motion in which the unknowns are the scaled magnetic flux through nonlinear elements and node potentials at parts of the circuit that contain linear magnetic materials. The scaling is based on per-unitization of variables and is needed to eliminate the wide disparity in magnitude of Jacobian matrix component values that is attributed to having both reluctance and permeance in the formulation. The proposed scaled structure is then shown to have the strong numerical performance of mesh-based MECs combined with the relatively straightforward derivation of nodal-based MECs. The numerical performance and derivation simplicity are demonstrated in a system that allows relative motion between components and is operated into a region of heavy saturation, under both static and dynamic operation.

APPENDIX

Fig. 11 shows the B - H characteristic of the ferromagnetic material. Fig. 12 shows the μ - B relationship, interpolated with splines of degree 1. In the same plot is the interpolated $\partial\mu/\partial B$ relationship, interpolated with splines of degree 0. Expressions for the airgap permeances as well as reluctance expressions for the magnets, stator teeth and rotor claws are developed herein. The reluctance expressions for the stator teeth and permanent magnets are taken directly from the rectangular geometry as:

$$R_{s1} = \frac{l_{stat}}{\mu_{s1}w_{stat}d_{sys}} \quad (52)$$

$$R_{s2} = \frac{l_{stat}}{\mu_{s2}w_{stat}d_{sys}} \quad (53)$$

$$R_m = \frac{t_{mag}}{\mu_0w_{root}d_{sys}} \quad (54)$$

The reluctance of each claw section is computed analytically by integrating differential reluctances where the permeability is assumed to be constant throughout a claw section. The differential reluctance of a claw section is given by

$$dR_{cXi} = \frac{dx'}{\mu_{cXi}w_i(x')d_{sys}} \quad (55)$$

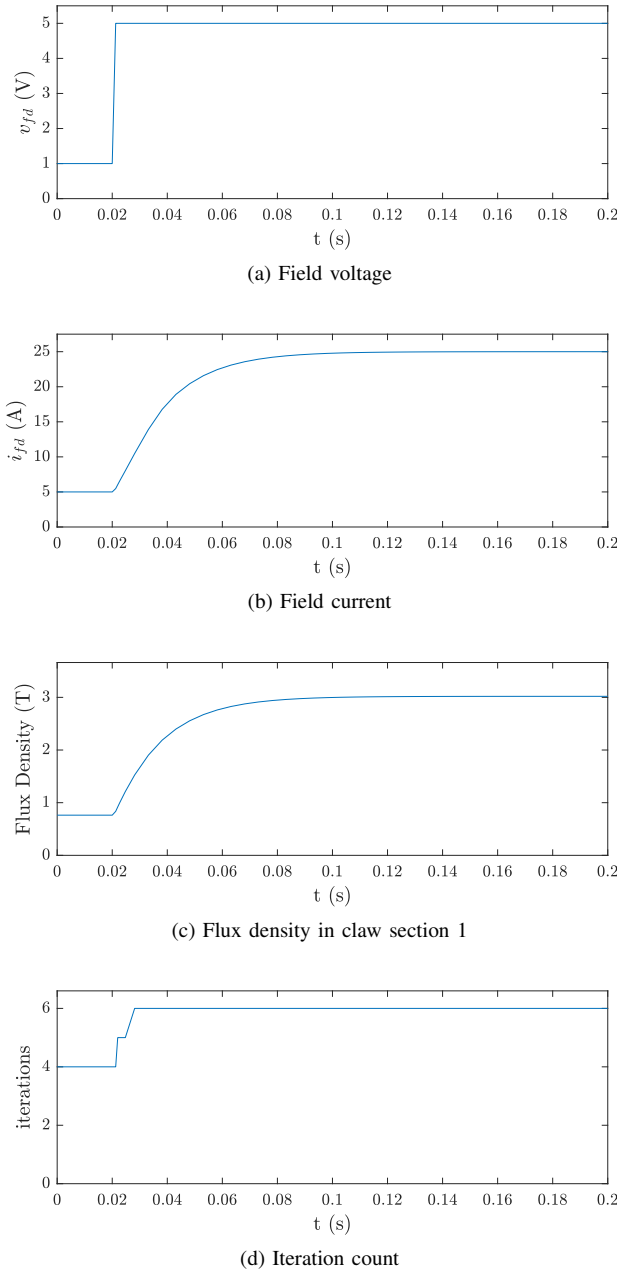


Fig. 10. Dynamic simulation: step change in field voltage.

where X is 1 or 2 indicating which claw half, and i ranges from 1 to N indicating the claw section. Referring to Fig. 13, the width of a claw section at a distance x' from the edge of the section can be expressed in terms of the width of the claw section at root and tip:

$$w_i(x') = N \frac{(w_{ri} - w_{ti})}{l_{claw}} x' + w_{ti} \quad (56)$$

Substituting the width of claw section i and integrating yields:

$$R_{cXi} = \frac{1}{\mu_{cXi} d_{sys}} \int_0^{\frac{l_{claw}}{N}} \frac{dx'}{w_i(x')} \quad (57)$$

$$R_{cXi} = \frac{l_{claw}}{\mu_{cXi} d_{sys} (w_{root} - w_{tip})} \ln \left(\frac{w_{ri}}{w_{ti}} \right) \quad (58)$$

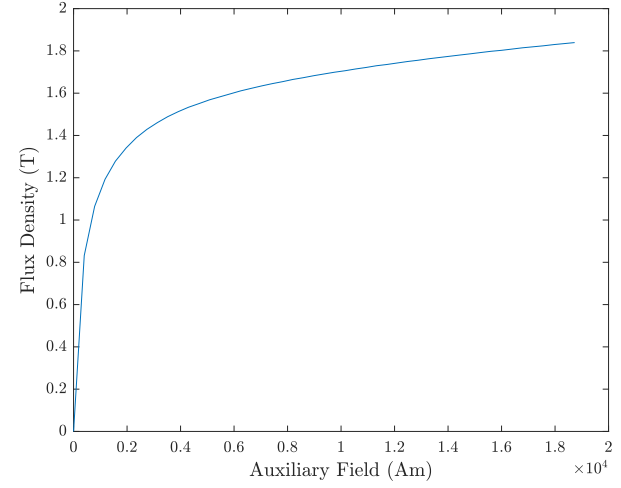


Fig. 11. B-H curve for magnetic materials.

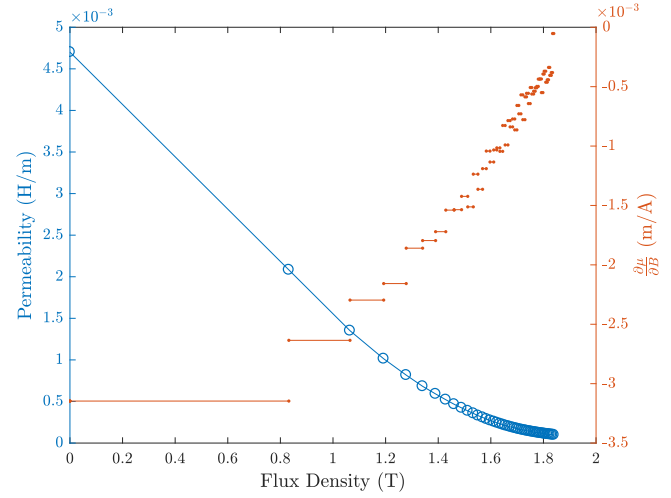


Fig. 12. μ - B and $\partial\mu/\partial B$ curve for magnetic materials.

where

$$w_{ri} = (w_{tip} - w_{root}) \cdot \frac{(i-1)}{N} + w_{root} \quad (59)$$

$$w_{ti} = (w_{tip} - w_{root}) \cdot \frac{i}{N} + w_{root} \quad (60)$$

for $i = 1 \dots N$. In order to accurately determine the permeability of claw sections during every iteration, the total flux in each nonlinear circuit element is divided by an effective area of each respective claw section. In this research, the cross-sectional area of claw section Xi is selected to be two-thirds of the way down the claw section, nearer to the tip of each claw section:

$$A_{cXi} = d_{sys} \left[(w_{tip} - w_{root}) \cdot \frac{(i-1/3)}{N} + w_{root} \right] \quad (61)$$

where again X is 1 or 2 indicating which claw half, and i ranges from 1 to N indicating the claw section. That is the cross-sectional area of claw section Xi is $d_{sys} w_i(x' = (1/3)l_{claw}/N)$ in reference to Fig. 13. A justification for this choice is provided in [13].

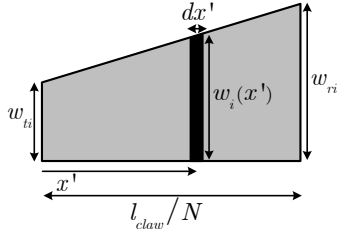


Fig. 13. Differential area of claws.

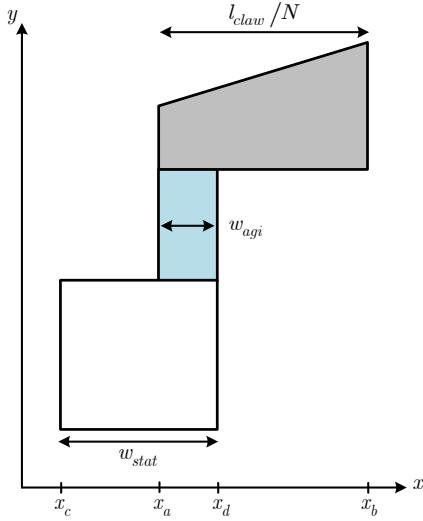


Fig. 14. Determining airgap flux tubes.

Airgap permeances are modeled in this research simply as rectangular flux tubes taking the direct path, neglecting fringing effects. The cross-sectional areas of the airgap flux tubes are dependent upon the relative alignment between claw sections and stator teeth. As shown in Fig. 14, the x -coordinates of the left and right edges of a claw section are denoted x_a and x_b , respectively. Similarly, the left and right edges of the stator tooth are denoted x_c and x_d respectively. Considering all cases of relative alignment, w_{agi} , the width of airgap flux tube i can be determined. In the example illustrated in Fig. 14, $w_{agi} = x_d - x_a$. The cross-sectional area of each airgap flux tube is then $A_{agi} = d_{sys}w_{agi}$. With knowledge of the cross-sectional area of each airgap element, the permeance of each airgap element can be evaluated as:

$$P_{agi} = \mu_0 \frac{A_{agi}}{g} \quad (62)$$

Logic statements are evaluated that consider all cases of relative alignment between each stator tooth edge and the claw section edges opposing them to form a total of $4N$ airgap elements

REFERENCES

- [1] V. Ostović, *Dynamics of Saturated Electric Machines*. Springer-Verlag New York, 1989.
- [2] T. A. Lipo, *Introduction to AC Machine Design*. University of Wisconsin, 2015.
- [3] S. D. Sudhoff, B. T. Kuhn, K. A. Corzine, and B. T. Branecky, "Magnetic equivalent circuit modeling of induction motors," *IEEE Transactions on Energy Conversion*, vol. 22, no. 2, pp. 259–270, June 2007.
- [4] M. Amrhein and P. T. Krein, "Induction machine modeling approach based on 3-d magnetic equivalent circuit framework," *IEEE Transactions on Energy Conversion*, vol. 25, no. 2, pp. 339–347, June 2010.
- [5] S. D. Sudhoff, *Power Magnetic Devices: A Multi-Objective Design Approach*. Wiley-IEEE Press, 2014.
- [6] M. Yilmaz and P. T. Krein, "Capabilities of finite element analysis and magnetic equivalent circuits for electrical machine analysis and design," in *2008 IEEE Power Electronics Specialists Conference*, June 2008, pp. 4027–4033.
- [7] M. Celebi, "Weight optimisation of a salient pole synchronous generator by a new genetic algorithm validated by finite element analysis," *IET Electric Power Applications*, vol. 3, no. 4, pp. 324–333, July 2009.
- [8] M. Bash and S. Pekarek, "Modeling of salient-pole wound-rotor synchronous machines for population-based design," in *2012 IEEE Power and Energy Society General Meeting*, July 2012, pp. 1–1.
- [9] M. L. Bash and S. Pekarek, "Analysis and validation of a population-based design of a wound-rotor synchronous machine," *IEEE Transactions on Energy Conversion*, vol. 27, no. 3, pp. 603–614, Sept 2012.
- [10] M. Ashabani and Y. A. R. I. Mohamed, "Multiobjective shape optimization of segmented pole permanent-magnet synchronous machines with improved torque characteristics," *IEEE Transactions on Magnetics*, vol. 47, no. 4, pp. 795–804, April 2011.
- [11] B. N. Cassimere and S. D. Sudhoff, "Population-based design of surface-mounted permanent-magnet synchronous machines," *IEEE Transactions on Energy Conversion*, vol. 24, no. 2, pp. 338–346, June 2009.
- [12] L. Yao, "Magnetic field modelling of machine and multiple machine systems using dynamic reluctance mesh modelling," PhD dissertation, Dept. Elect. Comput. Eng., Univ. Nottingham, Nottingham, U.K., 2006.
- [13] H. W. Derbas, J. M. Williams, A. C. Koenig, and S. D. Pekarek, "A comparison of nodal- and mesh-based magnetic equivalent circuit models," *IEEE Transactions on Energy Conversion*, vol. 24, no. 2, pp. 388–396, June 2009.
- [14] M. L. Bash, J. M. Williams, and S. D. Pekarek, "Incorporating motion in mesh-based magnetic equivalent circuits," *IEEE Transactions on Energy Conversion*, vol. 25, no. 2, pp. 329–338, June 2010.
- [15] L. O. Chua and P. Y. Lin, *Computer-Aided Analysis of Electronic Circuits: Algorithms and Computational Techniques*. Prentice Hall Professional Technical Reference, 1975.
- [16] G. Miscione, G. Antonini, and D. Frigioni, "A mixed nodal-mesh formulation of the peec method based on efficient graph algorithms," in *2008 IEEE International Symposium on Electromagnetic Compatibility*, Aug 2008, pp. 1–6.
- [17] C. Kelley, *Solving Nonlinear Equations with Newton's Method*. Society for Industrial and Applied Mathematics, 2003. [Online]. Available: <http://epubs.siam.org/doi/abs/10.1137/1.9780898718898>
- [18] R. Wang, S. Pekarek, M. L. Bash, A. Larson, and R. V. Maaren, "Incorporating dynamics in a mesh-based magnetic equivalent circuit model of synchronous machines," *IEEE Transactions on Energy Conversion*, vol. 30, no. 3, pp. 821–832, Sept 2015.
- [19] G. M. Shane and S. D. Sudhoff, "Design and optimization of permanent magnet inductors," in *2012 Twenty-Seventh Annual IEEE Applied Power Electronics Conference and Exposition (APEC)*, Feb 2012, pp. 1770–1777.
- [20] M. Johnson, M. C. Gardner, and H. A. Toliyat, "A parameterized linear magnetic equivalent circuit for analysis and design of radial flux magnetic gears – part i: Implementation," *IEEE Transactions on Energy Conversion*, vol. PP, no. 99, pp. 1–1, 2017.
- [21] I. Hasan, T. Husain, Y. Sozer, I. Husain, and E. Muljadi, "Analytical model-based design optimization of a transverse flux machine," in *2016 IEEE Energy Conversion Congress and Exposition (ECCE)*, Sept 2016, pp. 1–7.
- [22] B. du Peloux, L. Gerbaud, F. Wurtz, V. Leconte, and F. Dorschner, "Automatic generation of sizing static models based on reluctance networks for the optimization of electromagnetic devices," *IEEE Transactions on Magnetics*, vol. 42, no. 4, pp. 715–718, April 2006.
- [23] J. J. Lee, J. Lee, and K. S. Kim, "Design of a wfsm for an electric vehicle based on a nonlinear magnetic equivalent circuit," *IEEE Transactions on Applied Superconductivity*, vol. 28, no. 3, pp. 1–4, April 2018.
- [24] W. Peng and J. Gyselinck, "Combined magnetic-equivalent-circuit and finite-element modelling of switched reluctance machines," in *2016 IEEE International Energy Conference (ENERGYCON)*, April 2016, pp. 1–6.
- [25] V. Ostovic, J. M. Miller, V. K. Garg, R. D. Schultz, and S. H. Swales, "A magnetic-equivalent-circuit-based performance computation of a lundell alternator," *IEEE Transactions on Industry Applications*, vol. 35, no. 4, pp. 825–830, Jul 1999.

- [26] W. Kemmetmller, D. Faustner, and A. Kugi, "Modeling of a permanent magnet synchronous machine with internal magnets using magnetic equivalent circuits," *IEEE Transactions on Magnetics*, vol. 50, no. 6, pp. 1–14, June 2014.
- [27] V. Ostovic, "A novel method for evaluation of transient states in saturated electric machines," *IEEE Transactions on Industry Applications*, vol. 25, no. 1, pp. 96–100, Jan 1989.
- [28] C. Gear, "Simultaneous numerical solution of differential-algebraic equations," *IEEE Transactions on Circuit Theory*, vol. 18, no. 1, pp. 89–95, January 1971.



Daniel C. Horvath (S'13) received the B.S. degrees in Electrical Engineering and Computer Engineering in 2014, and the M.Sc. degree in Electrical Engineering in 2016, all from Purdue University, West Lafayette, IN. He is currently pursuing his Ph.D. degree in electrical engineering in the same university. His research interests include numerical electromagnetics, modeling of electric machinery, power electronics, and transportation electrification.



Steven D. Pekarek (S'89–M'96–SM'10–F'13) received his PhD in Electrical Engineering from Purdue University in 1996. From 1997-2004 Dr. Pekarek was an Assistant (Associate) Professor of Electrical and Computer Engineering at the University of Missouri-Rolla (UMR). He is presently the Nick Trbovich Professor of Electrical and Computer Engineering at Purdue University. He is an active member of the IEEE Power Engineering Society. He has served as the Technical Chair of the 2007 IEEE Applied Power Electronics Conference and

Technical Chair of the 2013 IEEE Electric Machines and Drives Conference. He is an Editor for the IEEE Transactions on Energy Conversion.



Scott D. Sudhoff (S'87–M'91–SM'07–F'08) received the B.S. (highest distinction), M.S., and Ph.D. degrees in electrical engineering from Purdue University in 1988, 1989, and 1991, respectively. From 1991-1993, he served as a consultant for P.C. Krause and Associates in aerospace power and actuation systems. From 1993 to 1997, he served as a faculty member at the University of Missouri - Rolla, and in 1997 he joined the faculty of Purdue University where he is the Michael and Katherine Birck Professor of Electrical and Computer Engineering. His interests include electric machinery, power electronics, marine and aerospace power systems, applied control, and evolutionary computing. Much of his current research focuses on genetic algorithms and their application to power electronic converter and electric machine design. He has published over one hundred papers in these areas, including six prize papers. He is a fellow of IEEE, served as Editor-in-Chief of IEEE Transactions on Energy Conversion, and currently serves as Editor-in-Chief of IEEE Power and Energy Technology System Journal.